Hydrodynamic Scaling of the Deceleration-Phase Rayleigh–Taylor Instability

Introduction

In inertial confinement fusion (ICF),[1] a shell of cryogenic deuterium (D) and tritium (T) filled with DT gas is imploded with direct laser illumination (direct drive)[2] or through an x-ray bath produced inside a laser-irradiated hohlraum (indirect drive).[3] Energy from the laser or x ray is absorbed in the plasma near the outer surface of the target, causing mass ablation. The ablation pressure pushes the shell inward by the "rocket effect." In addition to the Rayleigh–Taylor (RT) unstable outer surface during the acceleration phase, the inner surface of the shell is also unstable to the Rayleigh–Taylor instability (RTI) during the deceleration phase. The RT spikes stream into the hot spot, decreasing the burn volume and increasing the surface-to-volume ratio of the hot spot. This, in turn, increases the conduction losses,[4] resulting in a reduction in hot-spot temperature. The perturbations rapidly become nonlinear, and a significant fraction of the shell's kinetic energy is used to feed lateral motion, instead of contributing to the hot-spot pressure through radial compression.[5,6] The effective areal density ρR of the shell is expected to decrease and degrade the confinement time, burn volume, hot-spot pressure and temperature, and, therefore, the neutron yield. The yield-over-clean (YOC) is used as a measure of the effect of hydrodynamic instabilities on the implosion performance:[7]

$$\mathrm{YOC} = \left\{ \frac{\text{yield from exp or 3-D/2-D sim}}{\text{yield from 1-D sim}} \right\}. \qquad (1)$$

In an ICF implosion the initial nonuniformities arise because of ice roughness on the inner surface of the shell (which is usually greater than on the outer surface) and laser imprinting on the outer surface of the target.

The National Ignition Facility (NIF)[8] was built to perform 1.8-MJ (i.e., ignition-scale) indirect-drive implosions with 192 beams in a polar configuration. X-ray illumination was chosen because it was expected to improve target stability, but at the cost of a lower drive (i.e., reduced energy coupling to the target). Consequently, the stagnation pressure required for indirect-drive ignition is more than double that for direct drive with the same laser energy. Currently, the NIF is not configured to perform symmetric direct-drive illumination; therefore, it is being used in polar-direct-drive[9] mode to test direct drive. Polar direct drive is expected to achieve lower performance levels than symmetric drive. OMEGA[10] experiments, on the other hand, routinely use symmetric illumination, so extrapolating OMEGA to the NIF should be viewed as an upper bound of current NIF polar-direct-drive capabilities. Nevertheless, given the low NIF shot rate and high cost, extrapolating OMEGA experimental results to the NIF provides a very valuable tool for guiding future direct-drive experiments on the NIF.

The theory of hydrodynamic equivalence provides a way to extrapolate implosion performance on the OMEGA Laser System to ignition scales. Since scaling of the nuclear yield from an implosion ($Y \sim P_s^2 T_s \tau_b V_b$, where τ_b is the burnwidth and V_b is the neutron-averaged volume or *burn volume*) is dominated by the hot-spot pressure at stagnation P_s, the theory of hydro-equivalent scaling is developed keeping identical P_s for implosions with different driver energies. Unlike the pressure, the temperature at stagnation T_s is not scale invariant and is determined by considering the scaling of the hot-spot thermal conduction (see **Hydro-Equivalent Scaling of the Deceleration Phase**, p. 129). As described in Ref. 11, hydro-equivalent implosions designed to achieve the same stagnation pressure require equal values of the implosion velocity V_{imp}, shell adiabat α_0, and laser intensity I_L. A consequence of this choice of scaling is that the acceleration-phase RTI also scales hydro-equivalently if the initial seeds of the instability scale proportionally to the target radius R. A complete table of the one-dimensional (1-D) hydrodynamic scaling relations for ICF is listed in Ref. 11. The target dimensions (i.e., radius R and shell thickness Δ) and time t scale with laser energy E_L as

$$R \sim \Delta \sim E_L^{1/3}, \quad t \sim E_L^{1/3}, \qquad (2)$$

where $E_{L_{NIF}}/E_{L_\Omega} \approx 4^3$. Therefore, target sizes and laser pulse shapes for extrapolated direct-drive (NIF) ignition-scale implosions are 4× larger and longer than on OMEGA. The goal of this article is to examine the effect of the above hydrodynamic scaling on the deceleration-phase RTI and the hot-spot ignition condition.

Hot-Spot Dynamics and Hydrodynamic Equivalence

This section presents a model that describes the deceleration phase, starting from the hot-spot formation to the onset of ignition. The analysis is similar to that in Ref. 12. We also consider the effect of both losses and reabsorption of bremsstrahlung radiation. A fraction of the radiation energy emitted from the hot spot is reabsorbed at the hot-spot/shell interface; the remaining energy is treated as a loss. In the following subsections an analytic formulation of the hot-spot energy balance and mass ablation from the inner surface of the shell is developed; the effect of the radiation losses on the ignition condition is shown; the scaling of the deceleration-phase RTI is discussed; and the scaling of the YOC and the ignition condition is derived.

1. Hot-Spot Energy Balance

The hot-spot plasma is treated as an ideal gas with highly subsonic flows, and the hot-spot energy equation can be written as follows:

$$\frac{\partial}{\partial t}\left(\frac{p}{\Gamma-1}\right)+\nabla\cdot\left[\vec{u}\left(\frac{\Gamma p}{\Gamma-1}\right)\right]$$

$$=\nabla\cdot\kappa(T)\,\nabla T-\nabla\cdot\vec{F}+\frac{\theta\rho^2}{4m_i^2}\langle\sigma v\rangle\,\varepsilon_\alpha, \tag{3}$$

where $p(r,t)$, $\vec{u}(r,t)$, and $\rho(r,t)$ are the pressure, velocity, and density of the hot spot, respectively. Since the hot spot is subsonic $(\rho u^2 \ll p)$, the kinetic energy is small compared to the internal energy and has been omitted from the terms on the left-hand side. The ideal-gas adiabatic index Γ is 5/3 for DT gas. The first term on the right-hand side represents Spitzer thermal conduction $\kappa(T)=\kappa_0 T^v$, where $v = 5/2$ and $\kappa_0 = 3.7\times10^{69}$ m^{-1}s^{-1}J$^{-5/2}$ for $\ln\Lambda \approx 5$. Energy gained from fusion reaction is given by the third term, where θ is the fraction of total α-particle energy deposited in the hot spot, m_i is the average mass of DT ions, and ε_α (3.5 MeV) is the energy per α particle. The fusion reactivity follows $\langle\sigma v\rangle \approx C_\sigma T^3$ in the temperature range 3 to 8 keV with $C_\sigma \approx 2.6\times10^{-26}$ m^{3}keV^{-3}s^{-1}. The second term on the right-hand side of Eq. (3) represents the radiation losses, with $\vec{F}$ as the first moment of the radiation field over angle.[13] The bremsstrahlung emission from the hot spot integrated over all frequencies is given by

$$j = C_b\, p^2 T^{-3/2}, \tag{4}$$

where $C_b \approx 3.88\times10^{-29}\, Z^3/(1+Z)^2$ in J$^{5/2}$N^{-2}m s^{-1}, the pressure p is in N/m^2, temperature T is in joules, and j is in W/m^3. The ionization fraction Z is 1 for DT gas, with the assumption that there is no high-Z material mixed into the hot spot, which would considerably increase the bremsstrahlung losses. The subsonic hot-spot approximation applied to the momentum equation results in $p \approx p(t)$ (i.e., the hot spot is isobaric). The temperature of the low-density hot spot is much higher than the high-density shell, resulting in a self-similar solution for the hot-spot temperature given by[14]

$$T \approx T_c(t)\,f(\hat{r}) \quad \text{with} \quad f(\hat{r})=\frac{(1-\hat{r}^2)^{2/5}}{(1-0.15\hat{r}^2)}, \tag{5}$$

where $T_c(t)$ is the temperature of the hot spot's center and $\hat{r} = r/R_{hs}$ is the radial distance normalized to hot-spot radius R_{hs}. Bremsstrahlung radiation flux leaving a sphere of radius $\hat{r}$ calculated using Eq. (4) is given by

$$F(\hat{r})=\frac{C_b p^2 T_c^{-3/2} R_{hs}}{\hat{r}^2}\int_0^{\hat{r}} f^{-3/2}\hat{r}^2\,d\hat{r}, \quad \text{for } r < R_{hs},$$

$$F(\hat{r})=\mathcal{L}\frac{C_b p^2 T_c^{-3/2} R_{hs}}{\hat{r}^2}\,\frac{\mu_0}{3}, \quad \text{for } r > R_{hs}, \tag{6}$$

assuming that the low-temperature shell does not produce emission. Here,

$$\mu_0 = 3\times\int_0^1 f^{-3/2}\hat{r}^2\,d\hat{r} \approx 2.54$$

and $\mathcal{L}(t)$ is the fraction of emitted energy leaving the hot spot and shell.

The hot-spot energy equation was derived by integrating Eq. (3) from 0 to the hot-spot radius $R_{hs}(t)$. Since the shell velocity $(\dot{R}_{hs} \sim 350$ km/s$)$ is much greater than the ablation velocity ($V_{abl} \sim 10$ km/s), it was neglected; i.e., $u(R_{hs},t) = \dot{R}_{hs} - V_{abl} \approx \dot{R}_{hs}$. The hot-spot energy equation can be written in a dimensionless form as

$$\frac{d}{d\tau}\left(\hat{p}\hat{R}^5\right)=\gamma\hat{p}^2\hat{R}^5\hat{T}^\sigma-\beta_1\hat{p}^2\hat{R}^5\hat{T}^{-3/2}\hat{\mathcal{L}}(\tau), \tag{7a}$$

$$\gamma = \frac{\varepsilon_\alpha C_\sigma \mu_2}{24 c_k^{2+\sigma}} \left(\frac{p_s R_s}{V_{imp}}\right) T_*^{\sigma}, \tag{7b}$$

$$\beta_1 = \mathcal{L}_s \frac{2}{3} \mu_0 C_b \left(\frac{p_s R_s}{V_{imp}}\right) T_*^{-3/2}, \tag{7c}$$

with $\sigma = 1, c_k = 1.6\times10^{-16}$ J/keV, and $\mu_2 = 3\times\int_0^1 f\times\hat{r}^2\,d\hat{r} \approx 0.7$. The dimensionless variables [see Eqs. (8a) and (8b)] are written in terms of implosion velocity V_{imp} and adiabatic stagnation values for hot-spot radius R_s, pressure p_s, and central temperature T_s. The fraction of emitted energy that is lost $\mathcal{L}$ (or reabsorbed $\mathcal{R}$) is normalized to its value at stagnation $\mathcal{L}_s$ (or $\mathcal{R}_s$):

$$\tau = \frac{V_{imp}}{R_s} t, \quad \hat{p}(\tau) = \frac{p}{p_s}, \quad \hat{R}(\tau) = \frac{R_{hs}}{R_s},$$
$$\hat{\mathcal{L}}(\tau) = \frac{\mathcal{L}}{\mathcal{L}_s}, \quad \hat{R}(\tau) = \frac{\mathcal{R}}{\mathcal{R}_s}, \quad \hat{T}(\tau) = \frac{T_c}{T_*}, \tag{8a}$$

$$T_* = \left(\frac{25\mu_1}{36\kappa_0} p_s R_s V_{imp}\right)^{2/7}. \tag{8b}$$

In Eqs. (7), the parameter γ is proportional to the ratio of the fraction of α-particle energy deposited in the hot spot and the initial shell kinetic energy, and β_1 [also β_2 in Eqs. (10)] is proportional to the ratio of the bremsstrahlung energy emitted from the hot spot and the initial shell kinetic energy.

2. Hot-Spot Mass Ablation and Temperature Equation

The heat and radiation flux leaving the hot spot are recycled back as internal energy and PdV work on the material ablated from the inner surface of the shell (illustrated in Fig. 143.6). We consider that only a fraction of the emitted bremsstrahlung energy ($\mathcal{R}$) causes ablation, while the remaining fraction $\mathcal{L}$ is treated as a loss in energy [in Eq. (7a)]. Integrating Eq. (3) across the hot-spot boundary (or ablation front) as in Refs. 12, 14, and 15 and using the hot-spot mass ablation rate as $\dot{m}_{abl} = \rho V_{abl} = A p V_{abl}/T$ with $A = m_i/(1+Z)$ gives

$$\frac{5}{2A}\dot{m}_{abl} T_c R_{hs}^2 = \frac{6}{5}\kappa_0 T_c^{7/2} R_{hs} + \mathcal{R}(t)\frac{\mu_0}{3} C_b p^2 T_c^{-3/2} R_{hs}^3. \tag{9}$$

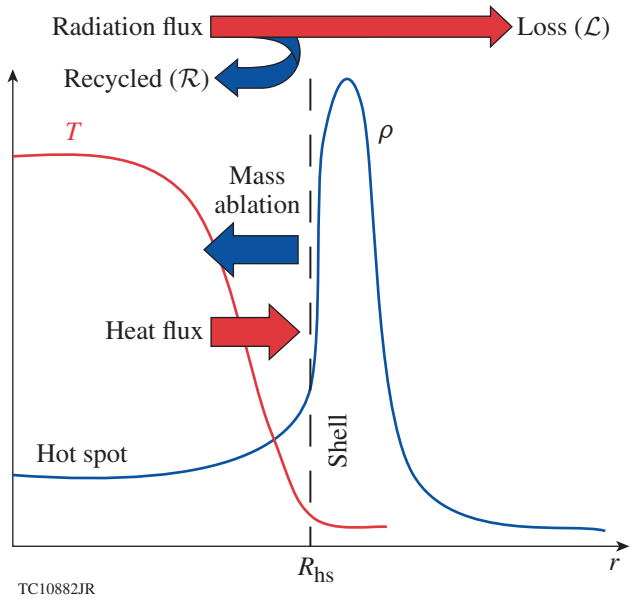

Figure 143.6
Density ρ and temperature T profiles during the deceleration phase of the implosion. The heat flux and a fraction of the emitted radiation energy are recycled back into the hot spot, causing mass ablation from the inner surface of the shell.

Equation (9) can be rewritten using the dimensionless variables in Eq. (8a) as

$$\frac{d}{d\tau}\left(\frac{\hat{p}\hat{R}^3}{\hat{T}}\right) = \hat{R}\hat{T}^{5/2} + \beta_2 \frac{\hat{p}^2\hat{R}^3}{\hat{T}^{5/2}}\hat{R}(\tau), \tag{10a}$$

$$\beta_2 = \mathcal{R}_s \frac{2\mu_0 C_b}{5\mu_1}\left(\frac{p_s R_s}{V_{imp}}\right) T_*^{-3/2}, \tag{10b}$$

where $\mu_1 = 3\times\int_0^1 f^{-1}\hat{r}^2\,d\hat{r} \approx 1.69$. The ablation velocity includes contributions from both thermal and radiative components. It was calculated by balancing the heat and radiation flux leaving the hot spot with the mass ablation on the inner surface of the shell:

$$V_{abl} = \frac{12A}{25}\frac{\kappa_0 T_c^{5/2}}{\rho_{shell} R_{hs}} + \frac{2A\mu_0}{15}\frac{C_b p^2 T_c^{-5/2} R_{hs}}{\rho_{shell}}\mathcal{R}(t). \tag{11}$$

Mass ablation into the hot spot increases the hot-spot density and reduces the temperature but has no effect on the pressure.[15]

3. Solution of the Ignition Model

The system of equations governing the deceleration phase includes the hot-spot energy equation, the hot-spot mass equation, and the equation of motion for the imploding shell. They are summarized as follows:

$$\frac{\mathrm{d}}{\mathrm{d}\tau}\left(\hat{p}\hat{R}^5\right) = \gamma\hat{p}^2\hat{R}^5\hat{T}^{\sigma} - \beta_1\hat{p}^2\hat{R}^5\hat{T}^{-3/2}\hat{\mathcal{L}}(\tau), \quad (12a)$$

$$\frac{\mathrm{d}}{\mathrm{d}\tau}\left(\frac{\hat{p}\hat{R}^3}{\hat{T}}\right) = \hat{R}\hat{T}^{5/2} + \beta_2\frac{\hat{p}^2\hat{R}^3}{\hat{T}^{5/2}}\hat{\mathcal{R}}(\tau), \quad (12b)$$

$$\frac{\mathrm{d}^2\hat{R}}{\mathrm{d}\tau^2} = \hat{p}\hat{R}^2. \quad (12c)$$

The last equation [Eq. (12c)] considers the shell to be an incompressible thin piston but with finite mass M_{sh}. The *thin-shell* approximation is discussed in Ref. 14 and is compared to the more-accurate *thick-shell* model in Ref. 15. Although the latter is more accurate, it is substantially complicated and leads to the same ignition-scaling relations (but different proportionality constants). Since the hydrodynamic scaling of the deceleration phase is the primary objective of this article, the thin-shell model is used. The stagnation values for R_{s}, p_{s}, and T_{s} are obtained by solving Eqs. (12) adiabatically, i.e., without α-energy deposition in the hot spot ($\gamma = 0$) and radiation ($\beta_1, \beta_2 = 0$). This leads to relations between the initial and stagnation parameters; the energy conservation requires that $M_{\mathrm{sh}}V_{\mathrm{imp}}^2 = 4\pi p_{\mathrm{s}}R_{\mathrm{s}}^3$ [from Eq. (12c)] and adiabatic compression requires $p(0)R(0)^5 = p_{\mathrm{s}}R_{\mathrm{s}}^5$ [from Eq. (12a)]. Rewriting Eq. (9) in dimensionless form as Eq. (10a) gives $T_* \approx 1.3\,T_{\mathrm{s}}$ [in Eq. (8b)]. The initial conditions $\hat{p}(0) = \varepsilon^{-5/2}$, $\hat{R}(0) = \varepsilon^{1/2}$, $\hat{T}(0) = \varepsilon^{-1/2}$, and $\dot{\hat{R}}(0) = -1$ are written in terms of the dimensionless parameter $\varepsilon = M_{\mathrm{sh}}V_{\mathrm{imp}}^2 \big/ 4\pi p(0)R(0)^3 \gg 1$, which is the ratio of the shell's kinetic energy and the hot spot's internal energy at the beginning of the deceleration phase (see Ref. 12). The thin-shell model overestimates the conversion of the shell's kinetic energy to the hot spot (i.e., 100% conversion); in order to limit this transfer, a heuristic finite shell-thickness correction (developed in Ref. 16) was used. Using this correction, the constants in Eqs. (7b), (7c), and (10b) can be rewritten in terms of $\rho\Delta$ (kg/m^2) of the shell and T_* (keV) as

$$\gamma = C_{\alpha}(\rho\Delta)^{3/4}T_*^{15/8}, \quad (13a)$$

$$\beta_1 = C_{\beta_1}(\rho\Delta)^{3/4}T_*^{-5/8},$$

$$\beta_2 = C_{\beta_2}(\rho\Delta)^{3/4}T_*^{-5/8}, \quad (13b)$$

where

$$C_{\alpha} = 1.77\times10^{-3}\,\mathrm{keV}^{-15/8}\,\mathrm{m}^{3/2}\,\mathrm{kg}^{-3/4},$$

$$C_{\beta_2} = \mathcal{R}_{\mathrm{s}}\times 0.327\,\mathrm{keV}^{5/8}\,\mathrm{m}^{3/2}\,\mathrm{kg}^{-3/4},$$

and

$$C_{\beta_1} = 2.75\times\left(\mathcal{L}_{\mathrm{s}}/\mathcal{R}_{\mathrm{s}}\right)C_{\beta_2}.$$

For a direct-drive ignition-scale target, the fraction of bremsstrahlung radiation energy reabsorbed by the shell is shown by the blue curve in Fig. 143.7; at stagnation, $\mathcal{R}_{\mathrm{s}}$ is 0.54 and $\beta_1 = 2.34 \times \beta_2$. The hot-spot model [Eqs. (12)] is solved numerically with a large value for ε ($\sim 10^4$). The solution for $\hat{p}$, $\hat{T}$, and $\hat{R}$ for a given value of β_1 becomes singular if γ exceeds a critical value γ_{ign}. The γ_{ign} curve shown in Fig. 143.8 is fit with a polynomial as

$$\gamma_{\mathrm{ign}} \approx 1.13 + 0.29\beta_1 + 1.89\beta_1^2. \quad (14)$$

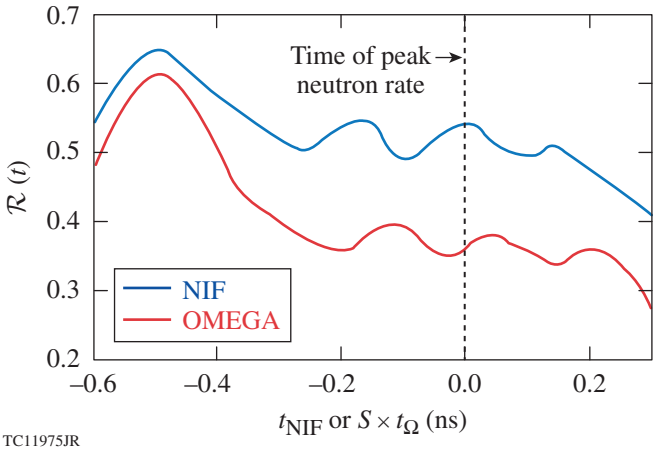

Figure 143.7
The fraction of emitted bremsstrahlung energy from the hot spot that is reabsorbed by the shell ($\mathcal{R}$) versus normalized NIF time ($S = 4$) is shown for the hydro-equivalent implosions on the NIF (blue) and OMEGA (red) scales. The remaining fraction of the emitted energy ($\mathcal{L}$) accounts for the radiation losses.

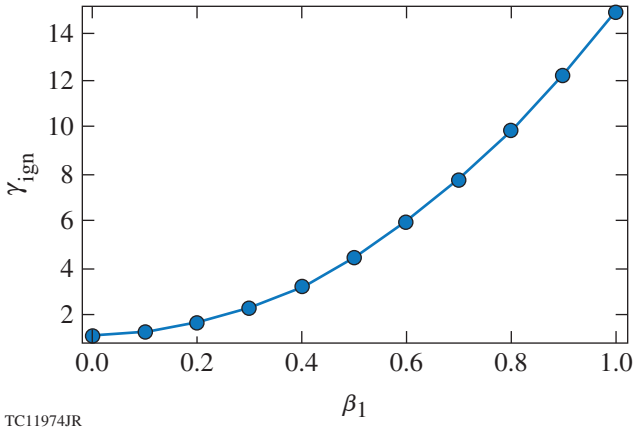

Figure 143.8
Plot of γ_{ign} versus β_1. When $\gamma \geq \gamma_{ign}$, the solution to Eqs. (12) becomes singular.

The analytic ignition parameter obtained from scaling [Eq. (13a)] can be normalized using the critical value from the model [Eq. (14)] and represented in terms of the no-α quantities; therefore, the no-α hot-spot–ignition condition is given by $\chi_{no\,\alpha} = \gamma/\gamma_{ign} \geq 1$. A more-elaborate compressible model (in Ref. 17) yields the same scaling as Eqs. (13a) and (14) but with different constants of proportionality. The scaling of the ignition parameter $\chi_{no\,\alpha}$ can be approximated (as first shown in Ref. 18) with

$$\chi_{no\,\alpha} \equiv (\rho R_n)^{0.8} \left(\frac{T_n}{4.7}\right)^{1.6} \mathrm{YOC}^{0.4}, \tag{15}$$

where ρR_n and T_n are the 1-D neutron-averaged areal density in g/cm^2 and temperature in keV, respectively, and a value of $\chi_{no\,\alpha} \geq 1$ implies hot-spot ignition. All the quantities in Eq. (15) are evaluated without α-particle deposition. Here, YOC is the ratio of the neutron yield from no-α two-dimensional (2-D) simulations and yield from no-α 1-D simulations. Since alpha heating is negligible in OMEGA implosions, the first step of an OMEGA-to-NIF extrapolation requires using the no-α performance (i.e., $\chi_{no\,\alpha}$). Based on the extrapolated value of $\chi_{no\,\alpha}$ for a NIF target, one can then determine the level of alpha heating on the NIF. If, after the extrapolation from OMEGA to the NIF, the value of $\chi_{no\,\alpha}$ is unity, one can then conclude that the NIF target would have ignited.

4. Hydro-Equivalent Scaling of the Deceleration Phase

In this section we consider the hydrodynamic scaling of the deceleration-phase RTI. The growth rate for the deceleration-phase RTI in the linear regime can be approximated with[19]

$$\Upsilon_{RT} = \alpha\sqrt{\frac{k\langle g\rangle}{1 + k\langle L_{min}\rangle}} - \beta k\langle V_{abl}\rangle, \tag{16}$$

where $\langle g\rangle$ is the average acceleration, $\langle L_{min}\rangle$ is the average minimum density-gradient scale length, $\langle V_{abl}\rangle$ is the average ablation velocity, and the coefficients α and β are 0.9 and 1.4, respectively. As shown in Ref. 20, increasing V_{abl} and L_{min} reduces the RTI growth rate and the unstable spectrum exhibits a cutoff around $\ell \approx 90$. The stabilizing terms depend on the thermal and radiation transport in the hot spot. The nepers of the deceleration-phase RTI scale as

$$N_e^{RT} = \alpha\sqrt{\frac{k\langle g\rangle t^2}{1 + k\langle L_{min}\rangle}} - \beta k\langle V_{abl}\rangle t$$

$$\sim \alpha\sqrt{\frac{\ell\left(c_{sh}^2/V_{imp}^2\right)}{1 + \ell\left(L_{min}/R_{hs}\right)}} - \beta\ell\left(\frac{V_{abl}}{V_{imp}}\right). \tag{17}$$

Equation (17) was written in dimensionless form using $k = \ell/R_{hs}$, $t \sim R_{hs}/V_{imp}$, and the sound speed in shell $c_{sh}^2 \sim P_{sh}/\rho_{sh}$. The inertia of the shell is balanced by the hot-spot pressure as $M_{sh}\ddot{R}_{hs} = 4\pi R_{hs}^2 P_h$ with $M_{sh} \sim \rho_{sh} R_{hs}^2 \Delta$; this was used to determine the scaling of the shell acceleration $\ddot{R}_{hs} \equiv g \sim \left(c_{sh}^2/R_{hs}\right)$. To determine the scaling of the stabilizing terms, i.e., $\left(V_{abl}/V_{imp}\right)$ and $\left(L_{min}/R_{hs}\right)$, it is necessary to determine the scaling of the thermal conduction and radiation transport in the hot spot and how they differ from the acceleration phase.

Thermal conduction, radiation, and α transports are typically modeled using diffusive terms. The diffusive terms in spherically converging geometry [i.e., $r^{-2}\partial_r\,(r^2\partial_r Q)$, where r is the radial coordinate and Q is the diffused quantity] can be written in the reference frame of the ablation front as

$$\frac{1}{(R_{abl} + \zeta)^2}\frac{\partial}{\partial\zeta}\left[(R_{abl} + \zeta)^2\frac{\partial}{\partial\zeta}Q\right], \tag{18}$$

where $\zeta = r - R_{abl}$, with R_{abl} representing the position of the ablation front. During the acceleration phase, the distance between the critical-density surface where the laser (or x-ray) energy is absorbed and the ablation front corresponds to the region where energy is diffused, i.e., $\zeta \sim (R_c - R_{abl})$. For

ICF implosions this distance is small compared to R_{abl}, i.e., $\left(\zeta/R_{abl}\right) \sim 0.1 \ll 1$. Therefore, the thermal diffusion term reduces to planar geometry [i.e., $\left(\partial^2/\partial\zeta^2\right)Q$] and the convergence effects can be neglected for the outer ablation-front surface. Therefore, the ablative stabilization term (derived in Ref. 11) can be written as $V_{abl}/V_{imp} \sim \dot{m}_{abl}(I_L)\alpha_0^{3/5}/P_{abl}^{3/5}(I_L)V_{imp}$, and the outer-surface ablative RTI scales hydro-equivalently as long as I_L, α_0, and V_{imp} are kept constant. Instead, during the deceleration phase, $\zeta/R_{abl} \sim 1$; therefore, the convergence effects are significant and the diffusive terms do not scale hydro-equivalently.

Using the scaling relation for the temperature at target center as $T_c \sim E^{0.07} \sim R^{0.21}$, the ablation velocity [Eq. (11)] scales with the target size as

$$\left(\frac{V_{abl}}{V_{imp}}\right) \sim \frac{\kappa_0 T_c^{5/2}}{\rho_{sh} R_{hs}} \sim \frac{1}{\sqrt{R}}. \tag{19}$$

The temperature scaling was first derived in Ref. 21 and can be retrieved analytically since $T_* \sim T_c \sim R^{2/7}$ from the temperature relation in Eq. (8b) (with V_{imp} and p_s as the constants in scaling). Equation (19) indicates that larger targets exhibit lower ablative stabilization. It will be shown in **Effect of Thermal Conduction: $\left(V_{abl}/V_{imp}\right)$ Scaling** (p. 133) that scaling of the ablative stabilization caused by $\left(V_{abl}/V_{imp}\right)$ is determined solely by thermal conduction, whereas scaling of the finite density-gradient scale-length stabilization $\left(L_{min}/R_{hs}\right)$ is determined by radiation transport (see p. 135). The Atwood number in Eq. (16) for finite L_{min} can be written as

$$A_T \equiv \frac{1}{1+kL_{min}} \sim \frac{1}{1+\ell\left(L_{min}/R_{hs}\right)}. \tag{20}$$

Reabsorption of radiation on the inner surface of the shell enhances the scale length such that $\langle kL_{min}\rangle \sim 1$ for $\ell < 60$ and $\langle kL_{min}\rangle \gg 1$ for $\ell > 60$. Therefore, it is useful to assess the scaling of radiation transport using $\left(L_{min}/R_{hs}\right)$ as the normalized scaling parameter. It is shown from simulations (see p. 135) that for NIF-like targets $\left(L_{min}/R_{hs}\right)_{NIF} \sim 0.1$, while for OMEGA targets $\left(L_{min}/R_{hs}\right)_{\Omega} \sim 0.07$. Since $\left[\left(L_{min}/R_{hs}\right)_{NIF}/\left(L_{min}/R_{hs}\right)_{\Omega}\right] \sim 1.5$, stabilization by L_{min} is enhanced for larger targets, which is an opposite trend compared to ablative stabilization.

Alpha-particle transport is not considered because the hot-spot–ignition condition $\chi_{no\,\alpha}$ uses no-α parameters. The alpha particles stopped within the hot spot augment the hot-spot temperature, and those leaking out of the hot spot deposit their energy on the inner shell surface, driving mass ablation. As shown in Ref. 22, both mechanisms enhance the ablative stabilization of the RTI. In a NIF-size target close to ignition, the stabilization of the RTI from alpha-driven ablation is significant. Even though we use a no-α extrapolation of $\chi_{no\,\alpha}$ from OMEGA to the NIF, the alpha-driven ablative stabilization is included through the value of the power index of the YOC [Eq. (15)]. This is discussed in Ref. 7, where it is shown that without ablative stabilization, the power index of the YOC would have been larger ($\approx$0.8). It is because of the ablative stabilization that the power index is reduced by half ($\approx$0.4), indicating that implosions close to ignition are less affected by the deceleration-phase RTI as the instability growth rates are reduced by alpha-driven mass ablation.

5. Hydro-Equivalent Scaling of the Yield-Over-Clean

The scaling of the Lawson parameter in Eq. (15) using $\rho R \sim E^{1/3}$ and $T \sim E^{0.07}$ can be written as

$$\chi_{no\,\alpha} \sim E^{0.38}\,\mathrm{YOC}_{no\,\alpha}^{0.4}. \tag{21}$$

The hydro-equivalent ignition condition on OMEGA considering $E_{NIF}/E_{\Omega} \sim 64$ is $\chi_{\Omega} = 0.21\left(\mathrm{YOC}_{\Omega}/\mathrm{YOC}_{NIF}\right)^{0.4}$. Since the normalized surface-roughness level on NIF targets is ~4× lower than on OMEGA targets, i.e., $\left(\sigma_{ice}^{\Omega}/R_{\Omega}\right)/\left(\sigma_{ice}^{NIF}/R_{NIF}\right) \sim 4$, the hydro-equivalent ignition condition on OMEGA improves (see Ref. 11) to

$$\chi_{\Omega} = 0.19\left(\frac{\mathrm{YOC}_{\Omega}}{\mathrm{YOC}_{NIF}}\right)^{0.4}. \tag{22}$$

The small improvement in the ignition condition from 0.21 to 0.19 occurs only by considering the above-mentioned surface roughness scaling and assumes equal growth factors between NIF and OMEGA during the deceleration phase. Here we also assumed that the laser imprint level on direct-drive OMEGA and extrapolated direct-drive ignition-scale implosions is equal. This choice refers to the most-stringent ignition condition on OMEGA (discussed in Ref. 11).

The yield degradation resulting from the deceleration-phase RTI can occur for two physical reasons: a reduction in the clean volume (i.e., volume within RT spikes) and a reduced coupling of the shell's kinetic energy to hot-spot pressure as the energy is used to drive the RTI. A simple estimate for the YOC, assuming a reduction of the clean volume only (i.e., without considering a drop in hot-spot pressure and temperature compared to without RTI), leads to

$$\mathrm{YOC} \sim \left(\frac{V_c}{V_{1\text{-D}}}\right) = \left(1 - \frac{\sigma_0 G_{RT}}{R_{1\text{-D}}}\right)^3, \tag{23}$$

where $R_{1\text{-D}}$ is the hot-spot radius in 1-D (i.e., without considering deceleration RTI), $V_c \sim (R_{1\text{-D}} - \sigma_0 G_{RT})^3$ is the hot-spot clean volume under the RTI spikes, σ_0 is the initial perturbation on the inner surface, and G_{RT} is the total growth factor of the RTI spikes into the hot spot. The YOC's from the implosions of the two scales (NIF and OMEGA) are related through the following equation:

$$\mathrm{YOC}_{\mathrm{NIF}} = \left[1 - \left(\frac{\sigma_0^{\mathrm{NIF}} G_{RT}^{\mathrm{NIF}}}{\sigma_0^{\Omega} G_{RT}^{\Omega}}\right)\left(\frac{R_{1\text{-D}}^{\Omega}}{R_{1\text{-D}}^{\mathrm{NIF}}}\right)\left(1 - \mathrm{YOC}_{\Omega}^{1/3}\right)\right]^3. \tag{24}$$

The ablative stabilization of the deceleration-phase RTI is different on the two scales, resulting in different growth factors. Simulations have been performed to determine the scaling of G_{RT} and YOC and to predict the hydro-equivalent ignition condition on OMEGA.

Hydro-Equivalent Implosion Design and Simulations of Deceleration-Phase RTI

This section describes the design and performance of the set of hydro-equivalent implosions used in this article. The 2-D simulations of the deceleration phase using the Eulerian radiation–hydrodynamics code *DEC2D/3D*[23–25] are also described.

The OMEGA-scale target shown in Fig. 143.9(a) is similar to those used in current cryogenic implosions performed on OMEGA.[26] This target had an 11-μm plastic (CD) ablator, 41 μm of DT ice, and a 431-μm outer radius. It was imploded with 27 kJ of laser energy, and when simulated with the 1-D hydrocode *LILAC*,[27] it achieved an implosion velocity of ~360 km/s with an average in-flight adiabat of 3. The hydro-equivalent NIF-scale target [Fig. 143.9(b)] was designed by scaling up the radius of each layer roughly by a factor of 4 since the laser energy was scaled 64× to 1.8 MJ. The NIF-scale target had a 35-μm-thick CD ablator, a 209-μm-thick DT ice layer, and a total radius of 1769 μm. The laser intensity I_L versus normalized time (t/t_{bang}) was kept unchanged [see Fig. 143.10(a)]. The time of peak neutron production, t_{bang}, was 11.42 ns and 2.83 ns for NIF and OMEGA implosions, respectively. The

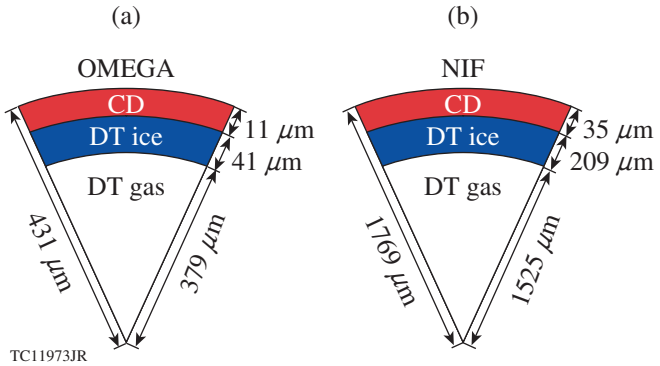

Figure 143.9
Target specifications for (a) an OMEGA-scale and (b) a NIF-scale cryogenic implosion simulation.

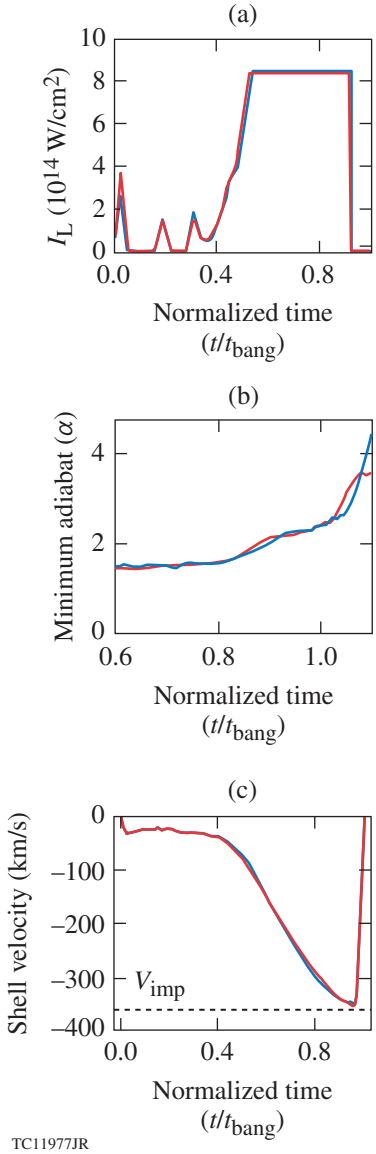

Figure 143.10
Time history of the essential hydrodynamic parameters (a) laser intensity I_L, and (b) fuel adiabat α, and (c) implosion velocity V_{imp} versus normalized time (t/t_{bang}) for the NIF-scale (blue) and hydro-equivalent OMEGA-scale (red) implosions.

target thickness had to be modified slightly to account for the nonscalable effects of radiation preheat in the acceleration phase. This arises because the radiation mean free path (ℓ_m) is the same in both target scales but the thickness of the ablator (CD) layer is 4× less on the OMEGA target, resulting in a lower preheat shielding. To keep the same fuel adiabat [see Fig. 143.10(b)] for implosions of different scales, some of the CD ablator was mass equivalently exchanged with DT ice for the larger targets.[11] The implosion velocity for targets of both scales is the same [shown in Fig. 143.10(c)]. The time evolution of the in-flight aspect ratio (IFAR) and the pressure profiles at stagnation P_s for the targets of both scales match closely (see Fig. 143.11), showing that the implosions are in accordance with the theory for 1-D hydro-equivalent scaling.[11] Energy in radiation flux leaving the hot-spot boundary [i.e., $(1/e)\rho_{max}$ and ρ_{max} (peak of shell density)] was measured. These measurements were used to calculate the fraction of emitted energy that was reabsorbed, $\mathcal{R}(t)$ (see Fig. 143.7), and the fraction that was lost, $\mathcal{L}(t)$. The minimum density-gradient scale length L_{min} and ablation velocity $V_{abl} = \left(\dot{M}_{hs} \big/ 4\pi R_{hs}^2 \rho_{shell}\right)$ at the inner surface of the shell were calculated. Radiation transport was turned on/off during the deceleration phase to study the individual effects of thermal conduction and radiation transport on the scaling of V_{abl} and L_{min}.

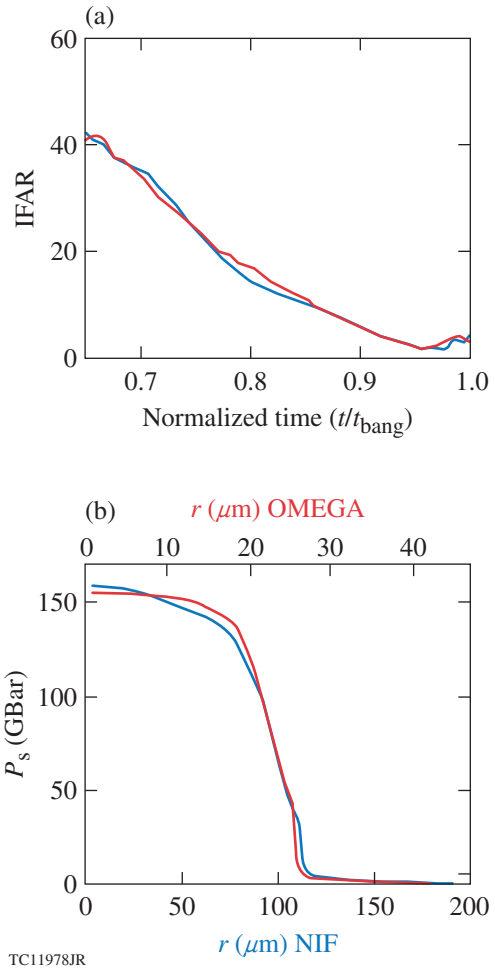

Figure 143.11
(a) In-flight aspect ratio (IFAR) versus normalized time (t/t_{bang}) and (b) pressure at stagnation (P_s) versus radial distance for the NIF-scale (blue) and hydro-equivalent OMEGA-scale (red) implosions.

The effects of the RTI on the deceleration phase of ICF implosions were studied using the hydrodynamic code *DEC2D/3D*.[25] The radial profiles of density, pressure, velocity, and temperature were extracted at the end of the acceleration phase (i.e., when the laser is turned off) from the 1-D NIF-scale simulation. The hydro-equivalent OMEGA profiles were generated by scaling down the size by a factor of 4, producing implosions with an exactly hydro-equivalent acceleration phase; therefore, an exclusive study of the scaling of the deceleration phase is possible. The profiles were mapped onto a 2-D high-resolution grid with single- or multimode velocity perturbations applied at the inner surface of the shell. The velocity perturbations were identical (i.e., hydro-equivalent) on both scales. The deceleration RTI developed at the unstable interface and degraded the implosion performance by reducing the clean volume. Thermal transport, α transport, and multigroup radiation transport were modeled as diffusion processes. Each of these can be turned on/off in the simulation. Since the no-burn case is considered in this article, the α-energy deposition was turned off. In **Effect of Thermal Conduction: $\left(V_{abl}/V_{imp}\right)$ Scaling** (see p. 133), radiation transport was turned off. The next subsection discusses results where both thermal and radiation transport processes were included.

The 2-D axisymmetric simulations (considering ϕ symmetry) were performed on a cylindrical x–z plane over a 90° wedge, with a high resolution of 900 × 900 grids for the hot spot and shell assembly on both scales. *DEC2D* is an Eulerian radiation–hydrodynamics code[23] with a moving mesh that shrinks radially with the average velocity and maintains a high resolution throughout the convergence during the deceleration phase (i.e., by a factor of ~3 to 5). The conservation equations are rewritten in a new dimensionless coordinate system $\xi = r/R(t)$ and $\zeta = z/Z(t)$, where $R(t)$ and $Z(t)$ are assigned functions of time. The computational domain is described by the Eulerian coordinates ξ and ζ varying between 0 and 1. There is no direct remapping involved. Since the actual spatial domain in r and z is compressed in time as a result of the prescribed inward motion of $R(t)$ and $Z(t)$, the high resolution

(900×900) is preserved throughout the real spatial domain for the entire simulation. The accuracy has been verified through convergence tests and is good enough to resolve modes up to $\ell = 100$. We use both a second-order centered MacCormack[28] scheme with artificial viscosity and second-order HLLC (Harten–Lax–Van Leer–Contact) Riemann solvers[29] without artificial viscosity. Earlier versions of *DEC2D* have been used to study the ablative stabilization of the deceleration-phase RTI in Refs. 15 and 20.

Single-mode simulations for a mode number ℓ varying from 2 to 68, with three different initial velocity perturbation amplitudes[7] ($\Delta V/V_{\text{imp}}$)—0.01%, 0.05%, and 0.1% of implosion velocity V_{imp}—were carried out. The $\Delta V/V_{\text{imp}}$ was chosen to keep the RTI within the linear regime. The time of peak neutron production, t_{bang}, was 1 ns after the laser was turned off on the NIF scale and 250 ps on the OMEGA scale. The single-mode growth factor was calculated as the ratio of the amplitudes at t_{bang} and at t_{bang}–800 ps into simulation on the NIF scale (or t_{bang}–200 ps on OMEGA).

Multimode simulations were carried out by including modes $2 \le \ell \le 68$. An ℓ^{-2} roll-off spectrum for mode numbers $\ell > 20$ and a constant amplitude for $2 \le \ell \le 20$ were used. Simulations were repeated by varying $\Delta V/V_{\text{imp}}$ from 0 (unperturbed) to 4%. The YOC $\left(\text{yield}_{\text{2-D}} \,/\, \text{yield}_{\text{1-D}}\right)$ was calculated for implosions on both scales. Simulations with an alternative ℓ^{-1} roll-off spectrum show good agreement with these results.

Non-Hydro-Equivalent Physics of the Deceleration Phase

The scaling of the deceleration-phase RTI is determined by scaling the stabilization resulting from mass ablation $\left(V_{\text{abl}}/V_{\text{imp}}\right)$ and density-gradient scale length $\left(L_{\text{min}}/R_{\text{hs}}\right)$, which can be understood by studying the effect of thermal conduction and radiation transport during this phase. This section presents the results from simulations and compares them to the analytic scaling.

1. Effect of Thermal Conduction: $\left(V_{\text{abl}}/V_{\text{imp}}\right)$ Scaling

The analytical scaling of $\left(V_{\text{abl}}/V_{\text{imp}}\right)$ shown in Eq. (19) can be rewritten using the radius and time-scaling factor $S \equiv R_{\text{NIF}}/R_{\Omega} = 4$ as

$$\frac{V_{\text{abl}}^{\text{NIF}}}{V_{\text{abl}}^{\Omega}} \sim \left(\frac{R_{\text{NIF}}}{R_{\Omega}}\right)^{-0.5} \sim 0.5. \tag{25}$$

On OMEGA the hot-spot mass density at stagnation ρ_s is higher and the hot-spot temperature T_s is lower than on NIF-scale implosions (see Fig. 143.12), leading to the 1-D scaling of hot-spot temperature as $T \sim R^{0.21}$. This can be attributed to the higher mass ablation rate on OMEGA, which is in qualitative accordance with Eq. (25). The pressure at stagnation P_s is the same on both scales, showing hydro-equivalence.

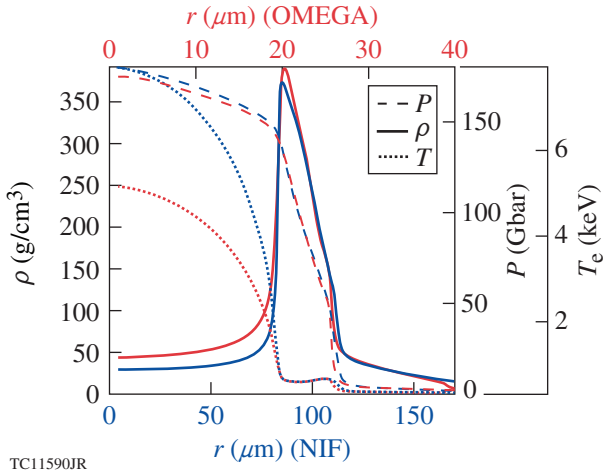

Figure 143.12
Pressure P, density ρ, and temperature T at time of peak neutron rate t_{bang} versus radial distance for NIF-scale (blue) and OMEGA-scale (red) implosions. Simulations were performed using the 1-D code *LILAC*, including thermal conduction (without radiation transport) during the deceleration phase.

The V_{abl} for the implosions of both scales is shown in Fig. 143.13(a). It is clearly seen that thermal conduction determines the scaling of ablation velocity $\left(\text{i.e., } V_{\text{abl}}/V_{\text{imp}}\right)$ because including radiation transport has no effect on the scaling of V_{abl} since it enhances the V_{abl} on both scales equally. Simulations show that

$$\left(\frac{V_{\text{abl}}^{\text{NIF}}}{V_{\text{abl}}^{\Omega}}\right)_{\text{no rad}} \sim \left(\frac{V_{\text{abl}}^{\text{NIF}}}{V_{\text{abl}}^{\Omega}}\right)_{\text{rad}} \sim 0.6, \tag{26}$$

which agrees with the analytical scaling in Eq. (25).

The normalized density-gradient scale length $\left(L_{\text{min}}/R_{\text{hs}}\right)$ arising from thermal conduction is rather small and has almost no effect on the scaling of the deceleration-phase RTI. From Fig. 143.13(b), considering the simulations without radiation, the normalized scale lengths at stagnation are $\left(L_{\text{min}}/R_{\text{hs}}\right)_{\text{NIF}} \sim 0.02$ and $\left(L_{\text{min}}/R_{\text{hs}}\right)_{\Omega} \sim 0.05$. Since $L_{\text{min}}/R_{\text{hs}} \ll 1$ on both scales, it affects only the very high ℓ modes that are already stabilized by ablation and has little effect on the scaling of the deceleration RTI [see Eq. (20)].

While the classical RTI (i.e., no ablation) is exactly hydro-equivalent [see Figs. 143.14(a) and 143.15(a)], the ablative stabilization caused by thermal transport does not scale hydro-equivalently [Fig. 143.14(b)] with the OMEGA target exhibiting higher stabilization.

To study the effect of $\left(V_{\text{abl}}/V_{\text{imp}}\right)$ scaling (i.e., thermal conduction) on the deceleration-phase RTI, a series of single-mode simulations without radiation transport (i.e., only thermal transport) for different ℓ numbers were carried out. Hydro-equivalent velocity perturbations with a single cosine mode were imposed on the inner surface of the shell. Short-wavelength modes exhibit higher ablative stabilization because of thermal conduction [see Eq. (17) and Fig. 143.15(b)]. The growth factors on the NIF are ~2.7× those on OMEGA, which is in agreement to the scaling in Eq. (17). Multimode simulations show that differences in the deceleration phase of hydro-equivalent implosions have an effect on the YOC ratio, with $\text{YOC}_{\Omega} > \text{YOC}_{\text{NIF}}$ by ~ 25% when the RTI becomes highly nonlinear (near saturation).

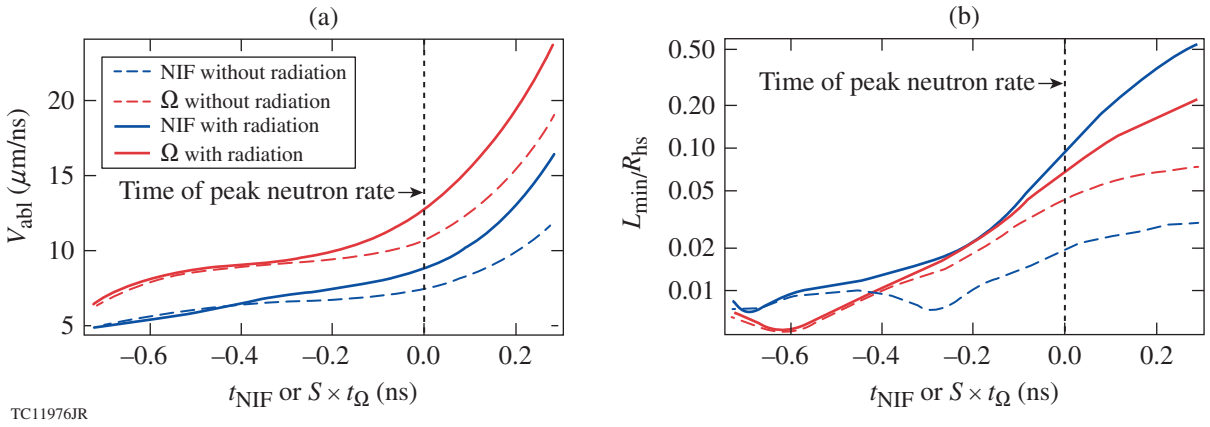

Figure 143.13
(a) Ablation velocity V_{abl} and (b) normalized density scale length $L_{\text{min}}/R_{\text{hs}}$ versus normalized NIF time ($S = 4$) for NIF (blue) and OMEGA (red) implosions. Simulations were performed using the 1-D code *LILAC*, with (solid lines) and without (dashed lines) radiation transport for the deceleration phase.

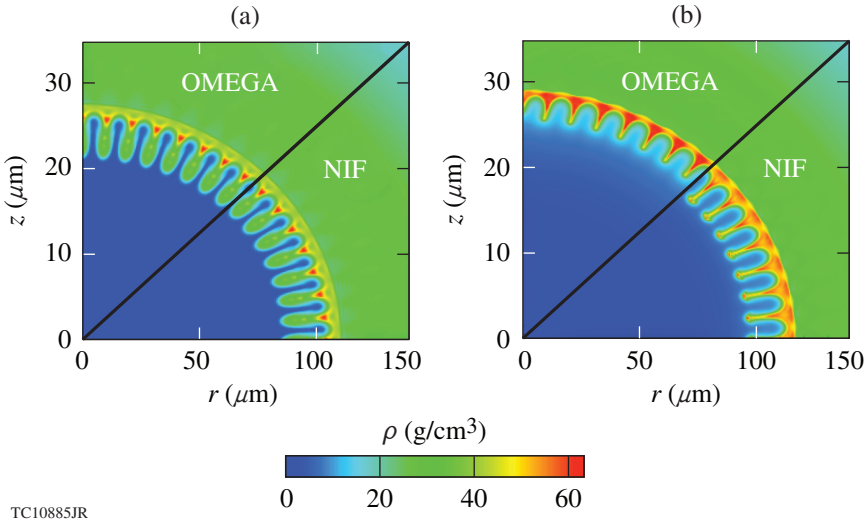

Figure 143.14
Density plots at hydro-equivalent times showing $\ell = 60$ deceleration RT growth on OMEGA (top half) and the NIF (lower half). (a) Simulations without thermal conduction on both scales match perfectly, illustrating that classical RTI is exactly hydro-equivalent. (b) Simulations with ablation caused by thermal transport (only) do not scale hydro-equivalently, resulting in different RT growth.

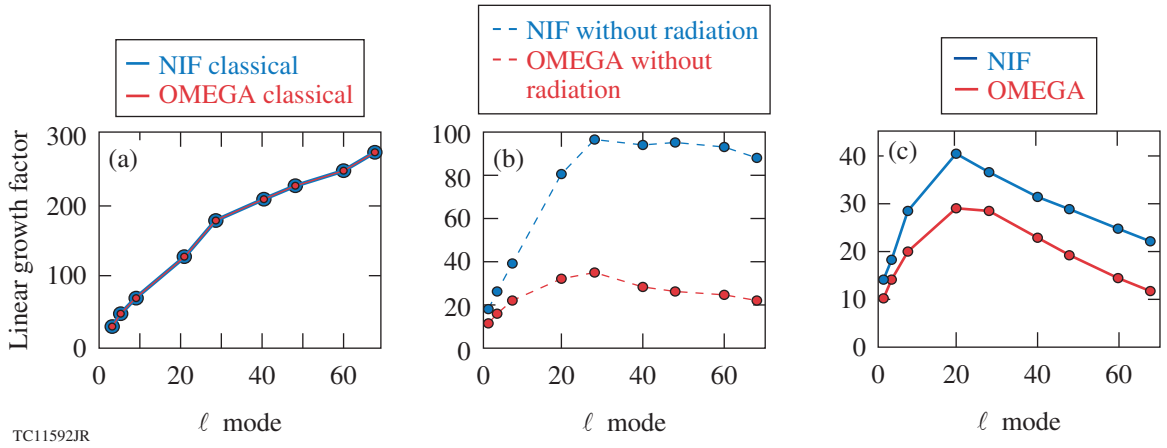

Figure 143.15
Deceleration-phase RTI linear growth factors versus mode number ℓ for NIF (blue) and OMEGA (red) hydro-equivalent implosions. (a) The classical growth factor, (b) growth factors with thermal transport (i.e., without radiation transport), and (c) growth factors with stabilization related to both thermal and radiation transport are shown.

2. Effect of Radiation Transport: $\left(L_{\min}/R_{\text{hs}}\right)$ Scaling

In this subsection we discuss the scaling of the RTI stabilization mechanism caused by reabsorption of bremsstrahlung emission from the hot spot. As the central plasma is heated by compression during the deceleration phase, it emits bremsstrahlung radiation. Some of the radiation emitted from the hot spot is absorbed on the inner surface of the shell, causing mass ablation and increasing $L_{\min}$ and V_{abl} during the last 400 ps (NIF-scale time) before bang time t_{bang} (see Fig. 143.13). The mean free path (mfp) of photons with energy $h\nu$ (in DT plasma) is given by the Kramers formula[13]

$$l \approx 2.25 \times 10^4 \frac{\sqrt{T}\,(h\nu)^3}{\rho^2}, \tag{27}$$

where l is in μm, the electron temperature T and photon energy $h\nu$ are in keV, and the density of plasma ρ is in g/cm^3. Photons emitted in a 5-keV hot spot exhibit an mfp of 2500 μm in the hot spot (considering a mass density of 50 g/cm^3) and an mfp of 20 μm in the cold (200-eV) shell with a mass density of 250 g/cm^3. The shell thickness for a typical NIF-scale target near stagnation is ~50 μm, whereas for a hydro-equivalent OMEGA target, the shell is 4× thinner (~12.5 μm). Consequently, more of the radiation emitted from the hot spot is reabsorbed by the NIF shell (see Fig. 143.7). The fraction of emitted energy that is reabsorbed by the shell at stagnation ($\mathcal{R}_s$) is greater on the NIF (0.54) than on OMEGA (0.36). As a result of higher reabsorption, the density-gradient scale length is more enhanced in the NIF target than in the OMEGA target (see Fig. 143.16). A quantitative mea-

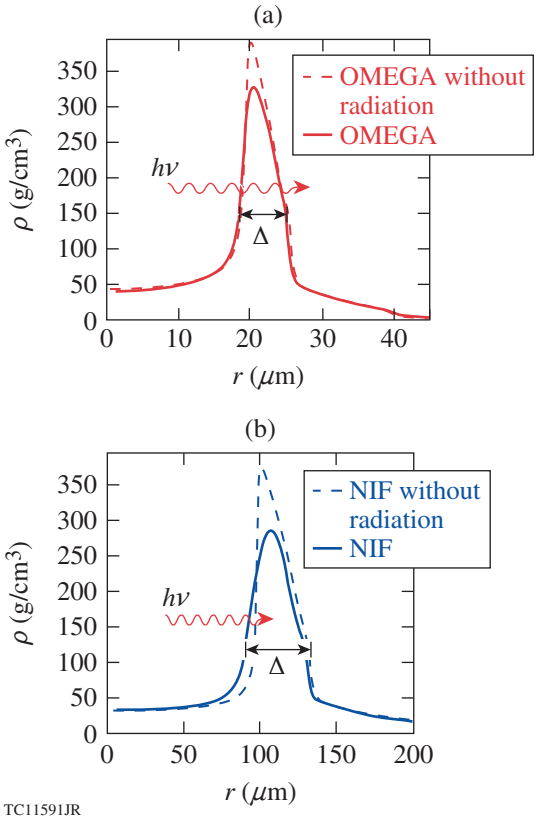

Figure 143.16
Density profiles at time of peak neutron rate for hydro-equivalent (a) OMEGA and (b) NIF implosions. It is shown that radiation reabsorbed by the NIF shell results in a greater enhancement of the scale lengths for the NIF with respect to the OMEGA target.

sure is provided in Fig. 143.13(b); by adding radiation transport to the simulations, the scale length $\left(L_{\min}/R_{hs}\right)$ increases by fivefold on the NIF scale, whereas the change is only a factor of 1.6 on OMEGA. Since there is a broad spectrum of emission frequency ν from the hot spot, the photons absorbed deeper in the shell enhance the density scale length; therefore, radiation transport determines the scaling of $L_{\min}$ in hydro-equivalent implosions:

$$\left(\frac{L_{\min}^{\text{rad}}}{L_{\min}^{\text{no rad}}}\right)_{\text{NIF}} > \left(\frac{L_{\min}^{\text{rad}}}{L_{\min}^{\text{no rad}}}\right)_{\Omega}. \tag{28}$$

A comparison of the central hot-spot temperatures for the simulations with and without radiation transport show that radiation transport has little effect on the scaling of the temperature with target size, unlike thermal conduction. The scaling of the temperature[21] with target size is $T_c \sim R^{0.28}$ without considering radiation transport, and it changes to $T_c \sim R^{0.21}$ when radiation transport is included.

The effect of the $\left(L_{\min}/R_{hs}\right)$ scaling on the linear RTI growth factors is shown in Fig. 143.15(c). The RTI on the NIF-scale implosion experiences higher stabilization from enhanced density gradients compared to OMEGA for the same initial perturbation $\Delta V/V_{imp}$. Similar studies on another target with a high implosion velocity (~430 km/s) showed identical trends. Comparing Figs. 143.15(b) and 143.15(c) shows that stabilization of the deceleration-phase RTI caused by ablation velocity $\left(V_{abl}/V_{imp}\right)$ and density scale length $\left(L_{\min}/R_{hs}\right)$ scales oppositely with target size. The stabilization related to V_{abl} is predominant on the smaller target, resulting in $\left(G_{RT}^{NIF}/G_{RT}^{\Omega}\right)_{\text{no rad}} \sim 2.7$, whereas the stabilization related to $L_{\min}/R_{hs}$ scales inversely and reduces the difference to $\left(G_{RT}^{NIF}/G_{RT}^{\Omega}\right)_{\text{rad}} \sim 1.35$. The impact of thermal conduction is more significant on the scaling of the RTI. The results of single-mode linear growth factors including both thermal conduction and radiation transport show that deceleration-phase RTI growth factors on NIF implosions are ~35% higher than on hydro-equivalent OMEGA implosions.

Scaling of the Ignition Condition

Multimode simulations (see Fig. 143.17) with hydro-equivalent initial perturbations (i.e., equal $\Delta V/V_{imp}$, described on p. 131) were used to calculate the $\text{YOC}_{\Omega}/\text{YOC}_{\text{NIF}}$ ratio [see Fig. 143.18(a)]. Increasing the nonuniformities results in higher YOC ratios, until the RTI becomes highly nonlinear (as in Fig. 143.17) and saturates at

$$\left(\frac{\text{YOC}_{\Omega}}{\text{YOC}_{\text{NIF}}}\right) \sim 1.17. \tag{29}$$

The scaling of the deceleration-phase RTI discussed in earlier sections is applicable to the linear and moderately nonlinear regimes of the instability. In the highly nonlinear regime the RTI saturates and this phase of the instability scales equivalently (from simulations); therefore, the YOC ratio asymptotes as shown in Fig. 143.18(a). This indicates that the opposite scaling of the ablative and radiative stabilization mitigates their effects on the capsule performance and makes the deceleration RTI almost effectively hydro-equivalent.

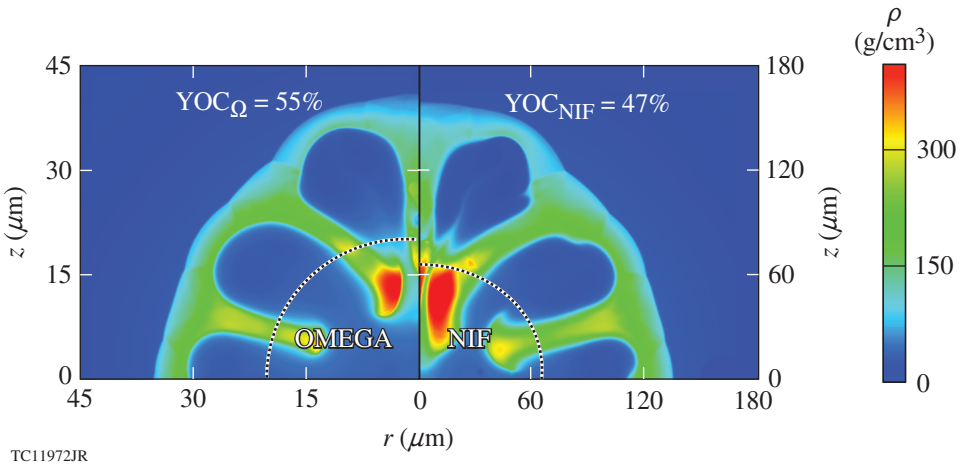

Figure 143.17
Contour plot of the density at bang time, showing nonlinear multimode RTI on NIF and OMEGA scales. The dashed line demarcates the fusion volume (or neutron-averaged volume); the YOC values for this set of hydro-equivalent simulations are indicated.

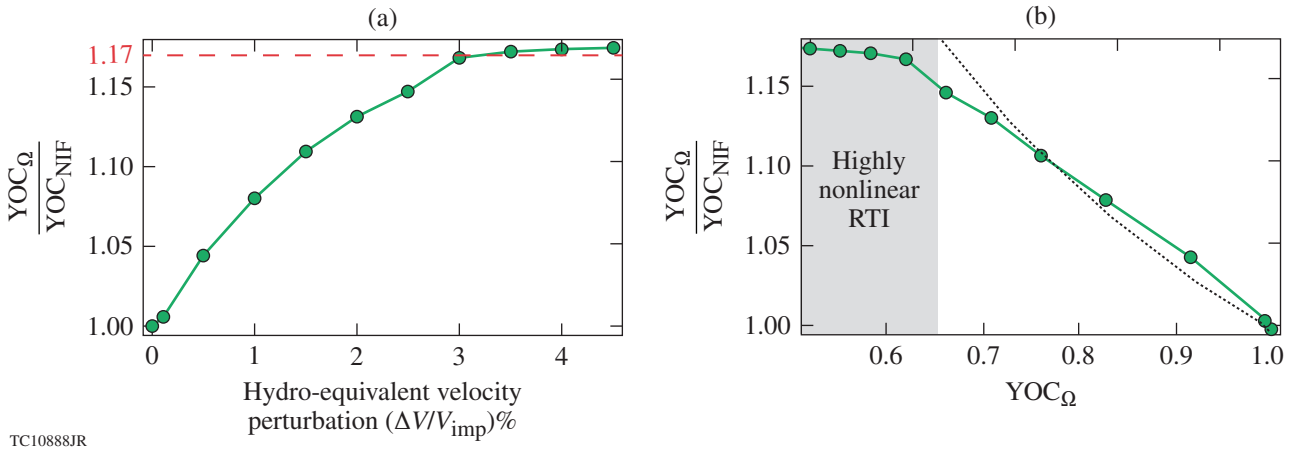

Figure 143.18
(a) Results from multimode simulations showing YOC ratio versus velocity perturbation for NIF- and OMEGA-scale implosions asymptote to 1.17 (red dashes). (b) $\left(\mathrm{YOC}_{\Omega}/\mathrm{YOC}_{\mathrm{NIF}}\right)$ versus YOC_{Ω} from *DEC2D* simulations of the deceleration phase (green solid line/circles) and analytic scaling (black dotted line) matches closely for the linear regime.

The analytic curve [shown in Fig. 143.18(b)] is obtained from Eq. (24) by varying the YOC_{Ω} and using a 35%-higher linear growth factor on the NIF (see **Hydro-Equivalent Scaling of the Yield-Over-Clean**, p. 130); the curve matches well with the multimode simulations in the linear regime and reproduces the YOC ratio of 1.17 obtained from simulations (for a YOC_{Ω} of 0.66, the calculated $\mathrm{YOC}_{\mathrm{NIF}}$ is 0.56). It is important to note that the formula in Eq. (24) assumes that the yield deterioration is caused by a reduction in the clean volume only; i.e., the hot-spot pressure and temperature are unaltered (compared to 1-D). In the highly nonlinear regime the YOC ratio obtained from simulations deviate from the linear theory [see Fig. 143.18(b)]. This can be attributed to the fact that for such highly nonlinear RTI, the conditions in the burn volume differ from the 1-D predictions because a significant fraction of the shell's kinetic energy is used to drive the instability instead of compressing the hot spot to higher pressures. This effect is being investigated by studying trends in neutron-averaged quantities from deceleration-phase simulations with nonlinear RTI. The scaling of the YOC with the burn average volume will be the subject of a forthcoming publication.

Using the above YOC ratio derived from considering the scaling of the stabilizing effects on the deceleration-phase RTI, the ignition parameter in Eq. (22) is given as $\chi_{\Omega} \approx 0.2$. This is in agreement with the analysis in Ref. 11 and valid within the frame of the 2-D analysis. While 3-D effects on the RTI may lead to a quantitative change of our conclusions, we do not expect any qualitative changes in the scaling results. A similar study in 3-D geometry is the focus of our current research and will be the subject of a forthcoming publication.

Conclusions

A comprehensive study of the scaling of the deceleration-phase RTI has been carried out to assess its impact on the YOC scaling and the hydro-equivalent ignition condition. An analytic model for the hot-spot–ignition condition has been developed, including the emission losses and reabsorption and mass ablation. It is shown that because of the convergence effects, the diffusive terms responsible for ablative stabilization (thermal conduction and radiation transport) do not scale hydro-equivalently with implosion size. Thermal conduction determines the scaling of the ablation velocity V_{abl} during the deceleration phase, and NIF implosions exhibit lower V_{abl} than hydro-equivalent OMEGA implosions. On the other hand, radiation emitted from the hot spot is more effectively reabsorbed by the thicker NIF shell, enhancing the density-gradient scale lengths $\left(L_{\mathrm{min}}/R_{\mathrm{hs}}\right)$ in NIF more than in OMEGA targets. Therefore, mitigation of the deceleration-phase RT instability caused by $V_{\mathrm{abl}}/V_{\mathrm{imp}}$ and $L_{\mathrm{min}}/R_{\mathrm{hs}}$ scale oppositely with target size. The linear growth factors on the NIF are 35% higher than on OMEGA. Considering both linear and nonlinear multimode simulations, it has been shown that the deceleration-phase YOC for OMEGA is ~17% higher than the YOC for NIF ignition-scale targets. A no-α Lawson ignition parameter of $\chi_{\Omega} \approx 0.2$ on OMEGA is required to achieve hydro-equivalent ignition for symmetric direct drive on the NIF.

ACKNOWLEDGMENT

The authors thank Dr. K. Anderson, Dr. J. A. Delettrez, and Dr. R. Epstein from the Laboratory of Laser Energetics and Prof. D. Shvarts from Ben-Gurion University of the Negev for many useful discussions. This work has been supported by the U.S. Department of Energy under Cooperative Agreement No. DE-FC02-04ER54789 (Fusion Science Center supported by

the Office of Fusion Energy Sciences) and DE-NA0001944 (National Nuclear Security Administration), the New York State Energy Research Development Authority, and the University of Rochester. The support of DOE does not constitute an endorsement by DOE of the views expressed in this article.

REFERENCES

1. J. Nuckolls *et al*., Nature **239**, 139 (1972).
2. S. E. Bodner, D. G. Colombant, J. H. Gardner, R. H. Lehmberg, S. P. Obenschain, L. Phillips, A. J. Schmitt, J. D. Sethian, R. L. McCrory, W. Seka, C. P. Verdon, J. P. Knauer, B. B. Afeyan, and H. T. Powell, Phys. Plasmas **5**, 1901 (1998).
3. J. D. Lindl, *Inertial Confinement Fusion: The Quest for Ignition and Energy Gain Using Indirect Drive* (Springer-Verlag, New York, 1998).
4. R. Kishony and D. Shvarts, Phys. Plasmas **8**, 4925 (2001).
5. B. K. Spears, M. J. Edwards, S. Hatchett, J. Kilkenny, J. Knauer, A. Kritcher, J. Lindl, D. Munro, P. Patel, H. F. Robey, and R. P. J. Town, Phys. Plasmas **21**, 042702 (2014).
6. A. L. Kritcher *et al*., Phys. Plasmas **21**, 042708 (2014).
7. P. Y. Chang, R. Betti, B. K. Spears, K. S. Anderson, J. Edwards, M. Fatenejad, J. D. Lindl, R. L. McCrory, R. Nora, and D. Shvarts, Phys. Rev. Lett. **104**, 135002 (2010).
8. E. I. Moses *et al*., Phys. Plasmas **16**, 041006 (2009).
9. S. Skupsky, J. A. Marozas, R. S. Craxton, R. Betti, T. J. B. Collins, J. A. Delettrez, V. N. Goncharov, P. W. McKenty, P. B. Radha, T. R. Boehly, J. P. Knauer, F. J. Marshall, D. R. Harding, J. D. Kilkenny, D. D. Meyerhofer, T. C. Sangster, and R. L. McCrory, Phys. Plasmas **11**, 2763 (2004).
10. T. R. Boehly, D. L. Brown, R. S. Craxton, R. L. Keck, J. P. Knauer, J. H. Kelly, T. J. Kessler, S. A. Kumpan, S. J. Loucks, S. A. Letzring, F. J. Marshall, R. L. McCrory, S. F. B. Morse, W. Seka, J. M. Soures, and C. P. Verdon, Opt. Commun. **133**, 495 (1997).
11. R. Nora, R. Betti, K. S. Anderson, A. Shvydky, A. Bose, K. M. Woo, A. R. Christopherson, J. A. Marozas, T. J. B. Collins, P. B. Radha, S. X. Hu, R. Epstein, F. J. Marshall, R. L. McCrory, T. C. Sangster, and D. D. Meyerhofer, Phys. Plasmas **21**, 056316 (2014).
12. C. D. Zhou and R. Betti, Phys. Plasmas **15**, 102707 (2008).
13. D. Mihalas and B. Weibel-Mihalas, *Foundations of Radiation Hydrodynamics* (Dover Publications, Mineola, NY, 1999).
14. R. Betti, M. Umansky, V. Lobatchev, V. N. Goncharov, and R. L. McCrory, Phys. Plasmas **8**, 5257 (2001).
15. R. Betti, K. Anderson, V. N. Goncharov, R. L. McCrory, D. D. Meyerhofer, S. Skupsky, and R. P. J. Town, Phys. Plasmas **9**, 2277 (2002).
16. R. Betti and C. Zhou, Phys. Plasmas **12**, 110702 (2005).
17. R. Betti, A. R. Christopherson, B. K. Spears, R. Nora, A. Bose, J. Howard, K. M. Woo, M. J. Edwards, and J. Sanz, Phys. Rev. Lett. **114**, 255003 (2015).
18. R. Betti, P. Y. Chang, B. K. Spears, K. S. Anderson, J. Edwards, M. Fatenejad, J. D. Lindl, R. L. McCrory, R. Nora, and D. Shvarts, Phys. Plasmas **17**, 058102 (2010).
19. H. Takabe *et al*., Phys. Fluids **28**, 3676 (1985).
20. V. Lobatchev and R. Betti, Phys. Rev. Lett. **85**, 4522 (2000).
21. C. D. Zhou and R. Betti, Phys. Plasmas **14**, 072703 (2007).
22. A. Schiavi and S. Atzeni, Phys. Plasmas **14**, 070701 (2007).
23. K. Anderson, R. Betti, and T. A. Gardiner, Bull. Am. Phys. Soc. **46**, 280 (2001).
24. A. Bose, P.-Y. Chang, J. R. Davies, and R. Betti, Bull. Am. Phys. Soc. **57**, 358 (2012).
25. K. M. Woo, A. Bose, R. Betti, J. A. Delettrez, K. S. Anderson, and R. Epstein, Bull. Am. Phys. Soc. **59**, 354 (2014).
26. T. C. Sangster, V. N. Goncharov, R. Betti, T. R. Boehly, D. T. Casey, T. J. B. Collins, R. S. Craxton, J. A. Delettrez, D. H. Edgell, R. Epstein, K. A. Fletcher, J. A. Frenje, V. Yu. Glebov, D. R. Harding, S. X. Hu, I. V. Igumenshchev, J. P. Knauer, S. J. Loucks, C. K. Li, J. A. Marozas, F. J. Marshall, R. L. McCrory, P. W. McKenty, D. D. Meyerhofer, P. M. Nilson, S. P. Padalino, R. D. Petrasso, P. B. Radha, S. P. Regan, F. H. Seguin, W. Seka, R. W. Short, D. Shvarts, S. Skupsky, V. A. Smalyuk, J. M. Soures, C. Stoeckl, W. Theobald, and B. Yaakobi, Phys. Plasmas **17**, 056312 (2010).
27. J. Delettrez, R. Epstein, M. C. Richardson, P. A. Jaanimagi, and B. L. Henke, Phys. Rev. A **36**, 3926 (1987).
28. R. MacCormack, J. Spacecr. Rockets **40**, 757 (2003).
29. E. F. Toro, *Riemann Solvers and Numerical Methods for Fluid Dynamics: A Practical Introduction* (Springer-Verlag, Berlin, 1999).